Regular Article

Ternary Z-scheme heterojunction of Bi_2WO_6 with reduced graphene oxide (rGO) and meso-tetra (4-carboxyphenyl) porphyrin (TCPP) for enhanced visible-light photocatalysis

Kai Hu [a,1], Changya Chen [a,1], Yuan Zhu [a,1], Guangming Zeng [a,*], Binbin Huang [a,*], Wenqian Chen [b], Shaoheng Liu [c], Chao Lei [d], Bisheng Li [a], Yang Yang [a]

[a] College of Environmental Science and Engineering, Hunan University and Key Laboratory of Environmental Biology and Pollution Control (Hunan University), Ministry of Education, Changsha 410082, PR China
[b] Department of Chemical Engineering and Technology, Imperial College London, Exhibition Road, London SW7 2AZ, UK
[c] College of Chemistry and Material Engineering, Hunan University of Arts and Science, Changde 415000, Hunan, PR China
[d] School of Hydraulic Engineering, Changsha University of Science & Technology, Changsha 410114, PR China

G R A P H I C A L   A B S T R A C T
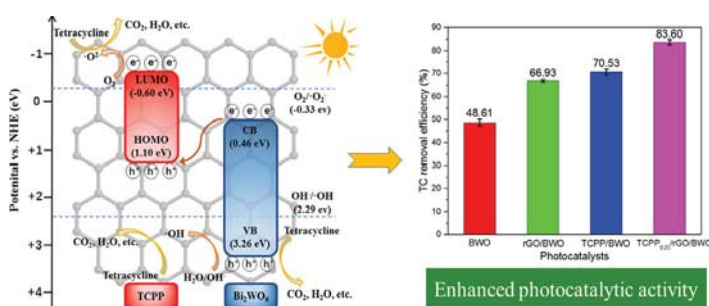
A R T I C L E   I N F O

A B S T R A C T

A highly efficient and new ternary $TCPP/rGO/Bi_2WO_6$ Z-scheme heterojunction was designed and fabricated via a facile hydrothermal approach and a liquid ultrasonic route in sequence. The crystal structures, morphologies, microstructures, chemical compositions, elemental states, optical and photo-electrochemical properties of the heterojunction were characterized. This Z-scheme $TCPP/rGO/Bi_2WO_6$ photocatalyst has significantly enhanced photocatalytic activity for the tetracycline (TC) degradation under the irradiation of visible light ($\lambda > 420$ nm) within 60 min, as compared to pure Bi_2WO_6, rGO/Bi_2WO_6 and $TCPP/Bi_2WO_6$ composites. The effects of the photocatalyst dosages, pollutant concentrations, coexisting ions and illumination conditions on the photodegradation were investigated. According to the trapping experiments and electron spin resonance analyses, the hole (h^+) and superoxide radical ($\cdot O_2^-$) mainly contribute to the TC decomposition in the $TCPP/rGO/Bi_2WO_6$ photocatalytic system. The photodegradation process in the $TCPP/rGO/Bi_2WO_6$ ternary composites can be well described by the proposed Z-scheme mechanism. The results indicate that more efficient charge separation, better light absorption, and larger surface area from the developed photocatalyst collectively contribute to the excellent photocatalytic performances. Besides, the photocatalyst has great stability and recyclability with a

* Corresponding authors at: College of Environmental Science and Engineering, Hunan University, Changsha, Hunan 410082, China.
E-mail addresses: zgming@hnu.edu.cn (G. Zeng), binbinhuang@hnu.edu.cn (B. Huang).
[1] These authors contribute equally to this article.

removal efficiency of 79.27% even after five times of repeated treatment. This work reports a new strategy for the preparation of Z-scheme heterojunction photocatalyst with high photocatalytic activity and provides an alternative for the effective removal of antibiotic wastewater through photocatalysis.

1. Introduction

Due to large scale industrialization and urbanization, environmental issues have become a very severe problem that threatens the safety of human life and hinders the sustainable development of society [1–5]. Photocatalytic oxidation is a new technology that uses photocatalysts to convert light energy into chemical energy, which subsequently lead to the generation of the hole (h^+), hydroxyl radical ($\cdot OH$) and superoxide radical ($\cdot O_2^-$) for the degradation of pollutants [6]. It has attracted increasing interest, since it, is recognized as one of the most effective approaches due to its superior properties of sustainable energy source, avoidance of secondary pollution, economical cost, and easy operation [7,8]. Since TiO_2 was discovered as the earliest photocatalyst, it has been widely used in the field of photocatalysis because of its strong oxidizing ability, non-toxicity, low cost and good photochemical stability [9,10]. However, TiO_2 can only absorb the ultraviolet light from approximate 4% of the solar spectral range, which results in the inefficient utilization of solar energy and greatly limits the photocatalytic performance and further application [11,12]. Therefore, it is necessary to explore new visible-respond photocatalysts.

Bismuth tungsten oxide (Bi_2WO_6) (BWO) is a typical Aurivillius oxide with perovskite layered structure constructed from alternating $(Bi_2O_2)^{2+}$ and WO_4^{2-} layers, which has been extensively investigated as effective photocatalysts over the years [13–15]. Firstly, the narrow energy gap of BWO (2.80 eV) means it has strong visible-light harvesting ability, which greatly improves the utilization efficiency of light energy as compared to TiO_2 [16,17]. In addition, BWO possesses a large surface area, and the interlayer space of the sandwich structure can provide sufficient active sites for photocatalytic reaction. The stable physicochemical properties of BWO also give it the ability to resist the photo-corrosion and to be recycled for many times. Although BWO exhibits excellent photocatalytic performances toward organic pollutant degradation, its photocatalytic activity is still limited by some factors. The maximum light absorption wavelength of BWO is only at around 460 nm, which means it still cannot fully utilize the solar energy [18]. Besides, most e^-–h^+ pairs recombine immediately after the photoexcitation, resulting in relatively low separation efficiency [19]. Among many proposed approaches, constructing heterojunction structure has been regarded as an effective approach and widely used to overcome the drawbacks of BWO in order to achieve better photocatalytic performance [20–24]. Therefore, choosing an appropriate material that matches well with BWO has become a key step in designing a highly efficient heterojunction photocatalyst.

Porphyrin is the main component of chlorophyll, which plays a central role in the photosynthesis of green plants. Inspired by the nature, porphyrin has been widely used as both appealing photosensitizers and effective electron donors in the photocatalytic hydrogen generation and contaminant degradation processes [25–28]. Among the various porphyrin molecules, meso-tetra (4-carboxyphenyl) porphyrin (TCPP) was chosen to couple with BWO to construct heterojunction photocatalyst in this work, mainly due to the following reasons: (1) benefiting from its conjugated macrocyclic π-electrons structure, TCPP possesses a narrow band gap and a wide photoabsorption range in visible-light spectral; (2) the lowest unoccupied molecular orbital (LUMO, −0.60 eV) and the highest occupied molecular orbital (HOMO, +1.10 eV) of TCPP is well-matched with the CB (+0.46 eV) and VB (+3.26 eV) of BWO to design a Z-scheme heterostructure, which will dramatically contribute to the separation of photoinduced e^-–h^+ pairs [29]; (3) TCPP has a high chemical stability and the carboxylic groups in TCPP make it combines with the BWO tightly [26]. However, no relevant information have been reported before.

Graphene is a two-dimensional material consisting of sp2-hybridized single-layer carbon atoms with excellent electrical conductivity, mechanical properties and large specific surface area [30–32]. To further enhance the photocatalytic activity of Z-scheme TCPP-BWO heterojunction, reduced graphene oxide (rGO) was incorporated into the system to produce ternary composites as excellent photocatalyst. The introduction of rGO not only enables the photocatalyst to better adsorb organic contaminants due to its π-π structure, but can also expand the visible-light response range by its great photo-response property [33]. Moreover, the high electron mobility of rGO can effectively restrain the e^-–h^+ recombination and promote their separation, thereby improving the photocatalytic performance of photocatalyst.

As a typical antibiotic, tetracycline (TC) has been widely used to treat diseases of human and many animals. Since only 30% TC can be absorbed by the organism, the remaining part enters the environment *via* urine and feces and extensively distributed in all kinds of water bodies [34]. On another hand, the residues of TC result in the generation of antibiotic-resistant pathogens and cause the transfer of antibiotic resistance genes, which pose serious threats to the human health and ecological safety [35]. Removing TC from the environment has become an urgent issue to be solved. Moreover, photocatalytic degradation of organic dye rhodamine B (RhB) has been extensively studied by a series of photocatalysts based on graphene/Bi_2WO_6 system (Table S1) [36–44], but few studies have been reported by using this system for the photocatalytic degradation of TC. Therefore, in this work, TC was selected as the targeted contaminant to evaluate the photocatalytic activity of the prepared catalyst under the illumination of visible light (>420 nm).

To the best of our knowledge, it was the first time to combine BWO, TCPP and rGO together to construct a Z-scheme TCPP/rGO/BWO heterojunction photocatalyst. In this work, the superior photocatalytic performance of TCPP/rGO/BWO was studied, and the effects of the photocatalyst dosages, pollutant concentrations, coexisting ions and illumination conditions on the photodegradation were carefully investigated. Moreover, the mechanism of the enhanced visible-light photocatalytic activity acquired by TCPP/rGO/BWO was explored in depth. We hope this work may provide a novel and efficient Z-scheme heterojunction photocatalyst for effective removal of antibiotic wastewater.

2. Materials and methods

2.1. Materials

Bismuth nitrate ($Bi(NO_3)_3 \cdot 5H_2O$), sodium tungstate ($Na_2WO_4 \cdot 2H_2O$), acetic acid (CH_3COOH), absolute ethanol (C_2H_6O) and tetracycline (TC) were purchased from Sinopharm (Shanghai, China). Meso-tetra (4-carboxyphenyl) porphyrin (TCPP) was obtained from Macklin (Shanghai, China). Graphene oxide dispersion (GO,

2 mg/mL) was acquired from Hengqiu (Suzhou, China). All chemical reagents were used without further purification. Mili-Q water was used throughout the study with a resistivity of 18 MΩ at room temperature.

2.2. Fabrication of photocatalysts

2.2.1. Fabrication of rGO/BWO

In a typical procedure, $Bi(NO_3)_3 \cdot 5H_2O$ (0.97 g) was dissolved in acetic acid (10 mL), followed by adding ultrapure water (30 mL) and graphene oxide dispersion (10 mL). The mixture was magnetic stirred for 30 min to prepare solution A. Meanwhile, $Na_2WO_4 \cdot 2H_2O$ (0.33 g) was added to ultrapure water (20 mL) to obtain solution B. Then, A was added into B dropwise before magnetic stirring for 1 h. The mixed solution was sealed in a 100 mL Teflon-lined stainless-steel autoclave and kept at 180 °C for 12 h, followed by cooling to room temperature naturally. Finally, the resultant solids were washed by absolute ethanol and ultrapure water for three times each, and then dried at 60 °C for 4 h in a vacuum oven and named as rGO/BWO (1.72 wt%). The pure BWO was also synthesized by hydrothermal method under the same conditions except the absence of GO.

2.2.2. Fabrication of TCPP/rGO/BWO

The TCPP/rGO/BWO composites were fabricated *via* a liquid ultrasonic route. Firstly, rGO/BWO (0.5 g) was added to absolute ethanol (40 mL) and ultrasonicated for 30 min to make it evenly dispersed. Next, a given amount of TCPP was added to this suspension and the mixture was ultrasonicated for 1 h. The mixture was then continuously stirred at room temperature until the solvent was completely volatilized. Finally, the solids were dried at 60 °C for 4 h in a vacuum oven. The as-prepared TCPP/rGO/BWO composites with 0.05, 0.10, 0.25, 0.50 and 0.75 wt% TCPP concentrations were recorded as $TCPP_{0.05}$/rGO/BWO, $TCPP_{0.10}$/rGO/BWO, $TCPP_{0.25}$/rGO/BWO, $TCPP_{0.50}$/rGO/BWO, and $TCPP_{0.75}$/rGO/BWO, respectively.

2.3. Characterization

The crystalline properties of the fabricated powders were measured by X-ray diffraction (XRD, D8 Advance, Bruker, Germany). The morphology and structure were observed by scanning electron microscopy (SEM, Supra55, Zeiss, Germany) and transmission electron microscopy (TEM, JEM-2100, JEOL, Japan), and the element constitution was detected by energy-disperse X-ray spectroscopy (EDS). The functional group of the samples was characterized by Fourier transform infrared spectroscopy (FT-IR, Nicolet 6700, Thermo Fisher, America). The surface chemical compositions and elemental states were analyzed by X-ray photoelectron spectroscopy (XPS, Escalab 250Xi, Thermo Fisher, America). The Brunauer–Emmett–Teller (BET) surface areas of as-prepared materials were measured using a surface area and porosity analyzer (Quadrasorb EVO, Quantachrome, America) by nitrogen adsorption–desorption. The optical properties of various photocatalysts were examined by UV–Vis diffuse reflectance spectra (UV–Vis DRS, UH4150, Hitachi, Japan). The existence of free radical during the photocatalytic reaction was confirmed by electron spin response (ESR, JES-FA200, JEOL, Japan) using 5,5-dimethyl-1-pyrroline N-oxide (DMPO) as spin-trapped reagent.

2.4. Photocatalytic experiments

The photocatalytic performance of the as-prepared catalysts was investigated by the photodegradation of TC by using a 300 W Xe lamp equipped with a cutoff filter (λ > 420 nm) as the light source. Typically, a photocatalyst (30 mg) was dispersed into a TC aqueous solution (15 mg/L, 100 mL) and constantly magnetic stirred for 30 min in the dark conditions to get the adsorption–desorption equilibrium and subsequently exposed to the illumination of visible light. Then, the solution (3 mL) was withdrawn from the system at predetermined interval time and centrifuged to remove the catalyst particles, and the TC concentrations were measured by detecting the maximum absorbance at 357 nm through an UV–vis spectrophotometer (UV-2700, Shimadzu).

The photodegradation efficiency of TC was assessed by the following formula:

$$\eta = \frac{C_0 - C_t}{C_0} \times 100\% \qquad (1)$$

where C_0 represents the initial TC concentration and C_t represents the TC concentration at time t, respectively.

2.5. Photo-electrochemical measurements

The photo-electrochemical measurements were conducted on electrochemical workstation through a standard three-electrode model with saturated calomel electrode as reference electrode, platinum filament as counter electrode and conductive glass coated with photocatalyst as working electrode, respectively. The three-electrode system was performed in 0.2 M Na_2SO_4 electrolyte solution and exposed to the illumination of visible light (>420 nm) provided by a 300 W Xe lamp. The detailed fabrication steps of the working electrode were as follows: 0.5% Nafion solution (1 mL) was prepared firstly and the material (10 mg) was dispersed into the liquid by half an hour of ultrasonication. Then 1 cm^2 area of 1.0 cm × 2.0 cm conductive glass was coated by the slurry and dried in an oven at 110 °C for 1 h.

3. Results and discussions

3.1. Characterization

3.1.1. XRD

The crystal structure of the as-synthesized BWO, rGO/BWO, TCPP/BWO and TCPP/rGO/BWO composites was characterized by XRD (Fig. S1). All the samples show eight diffraction peaks situated at 2θ = 28.33°, 32.80°, 47.19°, 55.83°, 58.61°, 68.82°, 76.08° and 78.50°, corresponding to the (1 1 3), (2 0 0), (2 2 0), (3 1 3), (2 2 6), (4 0 0), (3 3 3) and (2 4 0) crystal planes of orthorhombic phase Bi_2WO_6 (JCPDS card, No. 73-1126), which indicates the introduction of rGO and TCPP do not change the crystalline structure of BWO [45]. In addition, diffraction peaks belonging to GO are not found in the rGO/BWO and TCPP/rGO/BWO composites, probably due to the low amount and the reduction of GO, while similar observation was also found in the previous study [46]. Likewise, the XRD patterns of TCPP/BWO and TCPP/rGO/BWO composites do not show any characteristic diffraction peak of TCPP, which is attributed to the trace loading of TCCP on the supports. However, the intensity of diffraction peaks decreases slightly with the increasing TCPP content in the TCPP/rGO/BWO composites, indicating that the TCPP may have an adverse effect on the crystallinity of BWO crystal to some extent.

3.1.2. SEM, EDS and TEM

SEM, EDS and TEM were applied to investigate the morphologies, elementary compositions and microstructures of the as-prepared rGO/BWO and $TCPP_{0.25}$/rGO/BWO composites. It is observed that the rGO/BWO has a spherical morphology and a flower-like nanostructure with particle diameter of approximately 5.0 μm, which is composed of numerous crisscross nanoplates of BWO (Fig. 1a). The rough exterior texture of the BWO nanoplates
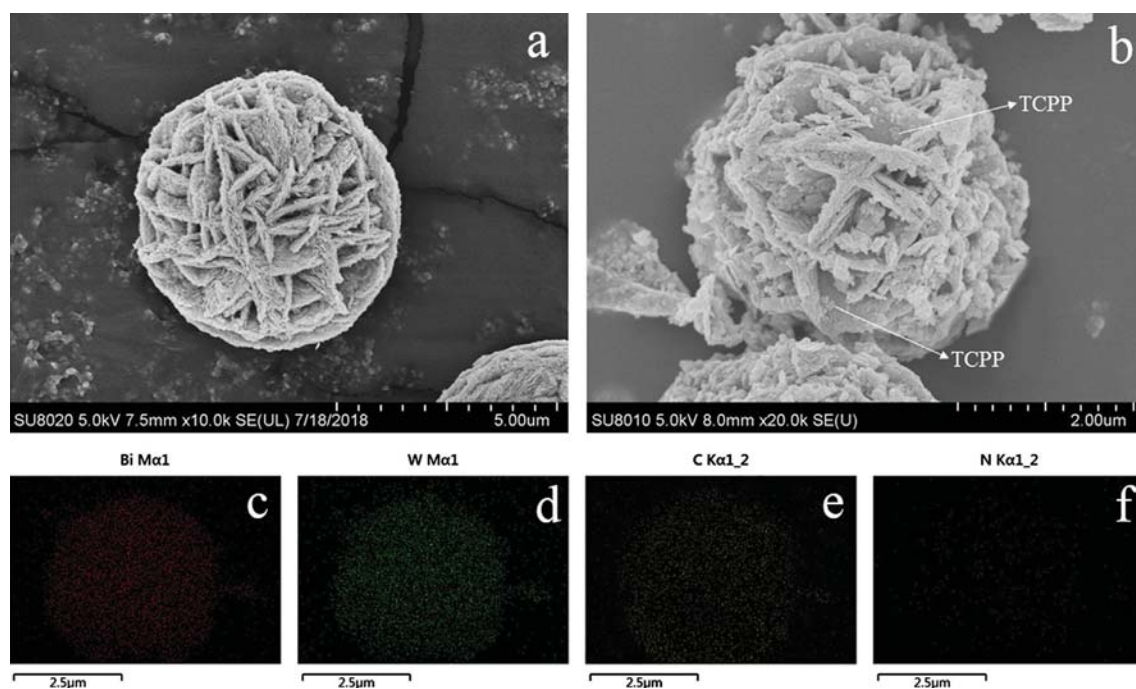
Fig. 1. SEM of (a) rGO/BWO, (b) $TCPP_{0.25}$/rGO/BWO, and (c–f) EDS mapping of $TCPP_{0.25}$/rGO/BWO.

is associated with the coverage of the stratiform rGO nanosheets. In addition, the numerous interstice and holes existing among the nanoplates are in favor of the penetration and absorption of light and the transport of reactive substrates [47]. After introducing TCPP, the $TCPP_{0.25}$/rGO/BWO remains the flower-like microsphere as well, whereas the BWO nanoplate substrates is partly coated with the smaller TCPP nanosheets (Fig. 1b). And some microspheres of rGO/BWO and $TCPP_{0.25}$/rGO/BWO composites were clearly observed in the low-magnification SEM images (Fig. S2). The EDS mapping analyses (Fig. 1c–f) demonstrate the co-existence and uniformly distribution of Bi, W, C and N elements in $TCPP_{0.25}$/rGO/BWO composites, which is highly consistent with the following XPS results (see below). Furthermore, the TEM image (Fig. 2a) clearly shows that $TCPP_{0.25}$/rGO/BWO is an individual microsphere, which agrees well with above SEM result. In the HRTEM image of $TCPP_{0.25}$/rGO/BWO (Fig. 2b), highly transparent graphene nanosheets can be observed at the edge of composite, indicating the successfully deposition of rGO onto the BWO nanoplates in the microsphere. The crystal lattice of BWO nanoplates with interplanar distances of 0.315 nm is assigned to the (1 1 3) lattice planes of BWO in $TCPP_{0.25}$/rGO/BWO [48]. The diffraction ring in the selective area electron diffraction (SAED) pattern of $TCPP_{0.25}$/rGO/BWO (inset of Fig. 2a) corresponds to the (1 1 3), (2 2 0), and (3 1 3) crystal planes of orthorhombic phase Bi_2WO_6, which is consistent with the XRD and HRTEM results. Therefore, the SEM, EDS and TEM characterization results confirm the successful preparation of the Z-scheme TCPP/rGO/BWO heterojunction photocatalyst.

3.1.3. FT-IR

FT-IR tests were performed to analyze the functional groups of samples and to confirm the presence of rGO and TCPP in the $TCPP_{0.25}$/rGO/BWO composites. Shown in Fig. S3 is the FT-IR spectra of pure TCPP, BWO, as well as rGO/BWO, TCPP/BWO and $TCPP_{0.25}$/rGO/BWO composites. In the spectrum of BWO, the typical peaks at 568.2 cm^{-1}, 727.9 cm^{-1} and 1386.8 cm^{-1} are ascribed to the Bi—O, W—O stretching vibration modes and W—O—W bridging stretching modes, respectively. These peaks are still present in

the rGO/BWO, TCPP/BWO and $TCPP_{0.25}$/rGO/BWO composites, indicating that no structural change of BWO occurred. The characteristic peaks at 1627.1 cm^{-1} and 1558.9 cm^{-1} appeared in the rGO/BWO composites are assigned to the C=O and C=C stretching mode of graphene, indicating the successful incorporation between BWO and rGO. The enhanced peaks at 727.9 cm^{-1} and 1386.8 cm^{-1} in the rGO/BWO composites are attributed to the interface interaction between BWO and rGO [49]. In the spectrum of the TCPP, the typical absorption bands in 600–1500 cm^{-1} are originated from the symmetrical and asymmetric stretching vibration of the pyrrole ring (i.e. v (N—N), v (C—N), v (C=C) and v (C=N)) [50]. Besides, the characteristic peaks at 1682.8 cm^{-1}, 1417.8 cm^{-1} and 1275.9 cm^{-1} are ascribed to the C=O, COO^- and —OH stretching vibrations, respectively, which indicate the existence of carboxyl group in the TCPP [51]. In the spectrum of TCPP/BWO composites, the new appeared peaks compared to the BWO at 1627.1 cm^{-1}, 1226.4 cm^{-1} and the enhanced peak at 1386.8 cm^{-1} are attributed to the red-shift of C=O, —OH and COO^- stretching vibrations, respectively, indicating that the BWO and TCPP have combined with each other successfully. In addition, the broad band at 3430.2 cm^{-1} appeared in all samples is related to the stretching vibrations of —OH. Furthermore, the FT-IR spectrum of $TCPP_{0.25}$/rGO/BWO composite inherit the features of both rGO/BWO and TCPP/BWO binary complexes, implying that the BWO, rGO and TCPP are coupled together perfectly to form the $TCPP_{0.25}$/rGO/BWO ternary composites. These results confirm the successful construction of the different rGO/BWO, TCPP/BWO and $TCPP_{0.25}$/rGO/BWO composites.

3.1.4. XPS

XPS analyses were carried out to reveal the chemical compositions and elemental states on the surface of pure BWO and $TCPP_{0.25}$/rGO/BWO composites. The full survey spectra (0–1100 eV) of both samples are shown in Fig. S4a, and Bi, W, O, C and N are indeed found in the $TCPP_{0.25}$/rGO/BWO composites. The high-resolution XPS spectra of Bi 4f, W 4f and O 1s for both BWO and $TCPP_{0.25}$/rGO/BWO, as well as C 1s and N 1s for only $TCPP_{0.25}$/rGO/BWO are employed. From the high-resolution Bi 4f
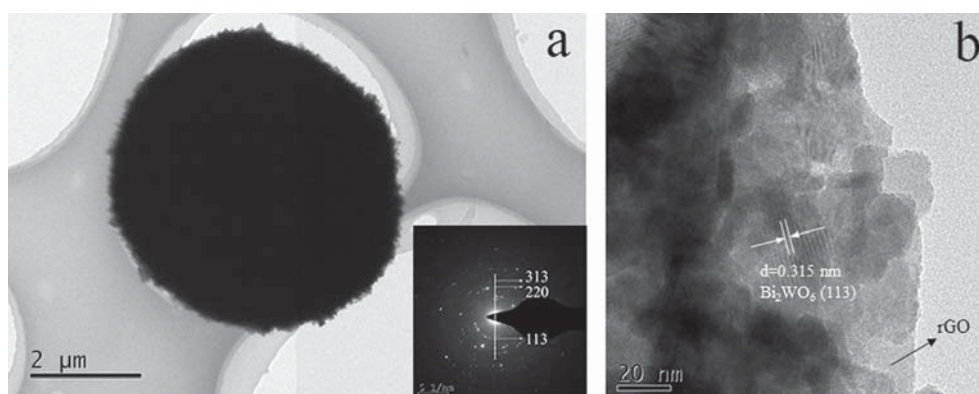
Fig. 2. (a) TEM, SAED and (b) HRTEM of TCPP$_{0.25}$/rGO/BWO.

spectrum in Fig. S4b, the binging energy situated at 158.7 eV and 164.0 eV are attributed to the Bi 4f$_{7/2}$ and Bi 4f$_{5/2}$, suggesting that the bismuth species exist as Bi^{3+} oxidation state in the BWO. Two peaks of W 4f located at 35.0 eV and 37.0 eV are corresponding to the W 4f$_{7/2}$ and W 4f$_{5/2}$, which are the characteristics of W^{6+} oxidation state in BWO phase (Fig. S4c). In the high-resolution O 1s spectrum, three individual peaks situated at 529.7, 531.8 and 533.2 eV belong to the lattice oxygen (Bi—O—W), the external hydroxyl groups (O—H), and the adsorbed oxygen species at the surface of BWO respectively (Fig. S4d) [52,53]. Compared to the pristine BWO, the peaks of Bi 4f, W 4f and O 1s over the TCPP$_{0.25}$/rGO/BWO composite all display an evident shift toward a high binding energy, suggesting the formation of strong chemical interactions among the BWO, rGO and TCPP. In the high-resolution C 1s spectrum, three fitting peaks situated at 284.6, 286.4 and 288.7 eV are attributed to the C—C, C—O and O—C=O bonds respectively (Fig. S4e) [46,54]. The weak peaks of C—O and C=O indicate that GO was well reduced to rGO after combining with BWO [55]. In addition, one main peak situated at 399.7 eV in the N 1s spectrum over the TCPP$_{0.25}$/rGO/BWO is assigned to the N element in the TCPP (Fig. S4f). The XPS result is in good accord with the FT-IR result, which further verifies that the TCPP$_{0.25}$/rGO/BWO composite has been successfully prepared.

3.1.5. BET

The nitrogen sorption isotherms of BWO, rGO/BWO and TCPP$_{0.25}$/rGO/BWO were carried out by BET analysis (Fig. S5a). According to the classification of IUPAC organization, all the isotherms can be categorized as type IV with a H$_3$ hysteresis loop, implying the presence of mesopores [56]. The corresponding Barrett–Joyner–Halenda (BJH) analyses (Fig. S5b) illustrate that most of the pores in the BWO, rGO/BWO and TCPP$_{0.25}$/rGO/BWO are mainly in the size range of 2–20 nm (especially at 4 nm). As shown in Table S2, the BET specific surface area is calculated to be 9.24, 13.08 and 16.15 m^2/g for BWO, rGO/BWO and TCPP$_{0.25}$/rGO/BWO respectively, while their corresponding pore volumes are measured to be 0.027, 0.033, and 0.043 cm^3/g. The results indicate that the introduction of rGO and TCPP can significantly enhance the surface area and pore volume of BWO. The large surface area and good porous structure of TCPP$_{0.25}$/rGO/BWO can provide more surface active sites and improve the transportation of the contaminant molecules and active radicals, which may result in the enhanced photodegradation ability of the TCPP$_{0.25}$/rGO/BWO composite [57].

3.1.6. Optical property

Optical properties of the pristine BWO, rGO/BWO, TCPP/BWO and TCPP/rGO/BWO composites with different contents of TCPP were measured by UV–Vis DRS (Fig. S6). The absorption edge of pristine BWO is approximately at 460 nm, while the incorporation of rGO successfully extends the light absorption to the visible light region. In addition, the traditional peaks of S-band at 420 nm and the four Q-bands at around 520, 560, 595 and 650 nm of TCPP are observed in all the TCPP modified composites, which confirms the successful introduction of TCPP again. Importantly, the TCPP/rGO/BWO composites show an even larger range of light absorption to the entire visible spectrum compared with the rGO/BWO, and the visible light absorption intensity of TCPP/rGO/BWO enhances with the increasing of TCPP. This result reveals that the construction of Z-scheme TCPP/rGO/BWO heterojunction can greatly improve the optical absorption, which provide a possibility to promote the generation of photo-induced electron-hole pairs and give rise to an enhanced photocatalytic activity.

Moreover, the band gap energy (E_g) of the pure BWO can be acquired from UV–vis DRS results according to the following formula [58]:

$$\alpha h\nu = A(h\nu - E_g)^{n/2} \tag{2}$$

where α represents the absorption coefficient, h is Planck constant, ν stands for the light frequency, $h\nu$ represents the energy of the incident photon, A is the proportionality constant, E_g represents the energy gap. Additionally, n is equal to 1 and 4 for a direct and indirect optical transition type of semiconductors, respectively. The n value of BWO is 1 [59,60], and the E_g of BWO is estimated to be 2.80 eV. Furthermore, the VB and CB of BWO can be determined by the following formula [61]:

$$E_{CB} = X - E^e - \frac{1}{2}E_g \tag{3}$$

$$E_{VB} = E_g + E_{CB} \tag{4}$$

where X represents the electronegativity of the semiconductor, which is calculated from the geometric average value of the electronegativity of constituent atoms in the semiconductor (6.36 eV for BWO) [62]. E^e stands for the energy of free electrons on the hydrogen scale (4.50 eV). E_g is the energy gap. Herein, applying the relevant data to the Eqs. (3) and (4), the CB and VB of BWO is calculated to be +0.46 eV and +3.26 eV.

3.2. Photocatalytic performance

3.2.1. Photocatalytic behavior of different materials

As depicted in Fig. 3a, the photocatalytic activities of different materials developed in this study were investigated by the photodegradation of TC. The TC was hardly removed in the blank test without the addition of photocatalyst and hence the effect of TC
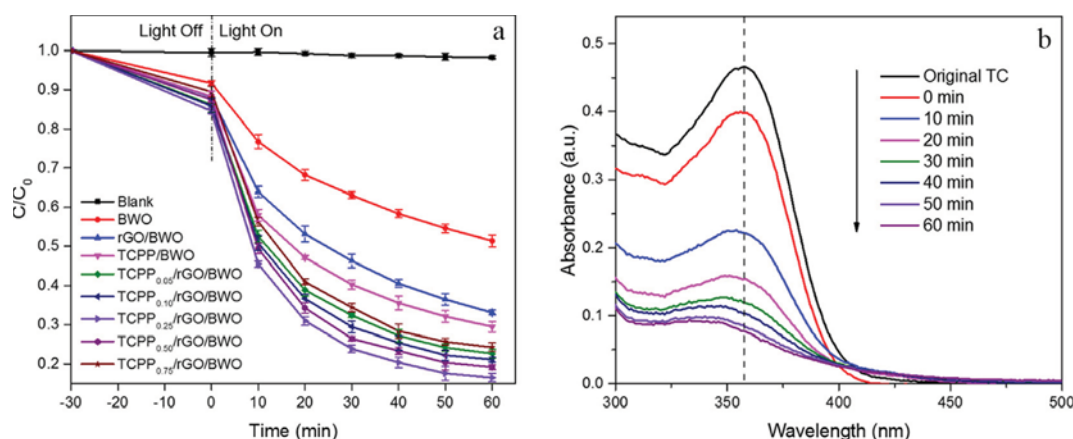
Fig. 3. (a) Photodegradation of TC by pure BWO, rGO/BWO, TCPP/BWO and TCPP/rGO/BWO with different TCPP contents under visible-light illumination; (b) the absorbance variation curves during the photodegradation of TC by the TCPP$_{0.25}$/rGO/BWO composite under visible-light illumination.

photolysis on the photocatalytic degradation reaction can be neglected. As shown in Fig. S7, the adsorption capacity of TC on BWO, rGO/BWO and TCPP$_{0.25}$/rGO/BWO was enhanced in turn because of the increased surface area and pore volume, and the adsorption equilibrium was achieved within 30 min in the darkness. After the start of illumination, the TC concentration in all the photocatalysis experiments gradually decreased with time. In particular, the photocatalytic performances of rGO/BWO (66.93%) and TCPP/BWO (70.53%) binary composites were significantly higher than BWO counterpart (48.61%) within 1 h of visible-light irradiation. More importantly, all the TCPP/rGO/BWO ternary composites with different TCPP contents had an even better photocatalytic efficiency under the same conditions. The catalytic performance was enhanced when the TCPP content was increased from 0.05% to 0.25% and the TCPP$_{0.25}$/rGO/BWO had the highest photodegradation efficiency of 83.60%. Furthermore, the variation of absorbance curve during the photodegradation of TC over TCPP$_{0.25}$/rGO/BWO composite was also recorded. As shown in Fig. 3b, the absorbance of TC significantly decreased with the increased illumination time. This can be attributed to the enhanced adsorption capacity for TC and the better utilization of light energy, as well as the higher separation efficiency of the photoexcited charge carriers. However, the photocatalytic performance started to decrease with the further increasing of TCPP content. It can be due to the covering of active sites on the surface of BWO by the redundant TCPP, resulting in the decrease of the photocatalytic activity of TCPP/rGO/BWO composites. The complete decomposition of TC was investigated by TCPP$_{0.25}$/rGO/BWO under visible-light illumination. As shown in Fig. S8, the degradation rate of TC gradually decreased with the prolongation of time and the complete removal of TC was ultimately achieved in 360 min, which is mainly due to the competition effect between the accumulated intermediates and TC molecules during the photocatalysis process. In addition, another typical antibiotic ciprofloxacin (CIP) was chosen to further test the catalytic activity of BWO, rGO/BWO and TCPP$_{0.25}$/rGO/BWO, and the result suggests that TCPP$_{0.25}$/rGO/BWO also had an excellent photocatalytic performance for CIP degradation compared to the BWO and rGO/BWO. (Fig. S9).

3.2.2. Effect of photocatalyst dosages

The amount of photocatalyst used in an application is an important factor related to both the photocatalytic performance and the economic cost. As shown in Fig. 4a, a series of photocatalyst dosages (from 0.10 g/L to 1.00 g/L) were chosen to investigate their influence on the photocatalytic performance. The photodegradation efficiency of TC rapidly increased from 61.89% to 83.60% when

the dosages of TCPP$_{0.25}$/rGO/BWO increases from 0.10 g/L to 0.30 g/L. When the catalyst dosage continued to increase to 0.50 g/L, the degradation efficiency was only slightly increased to 85.36%. Nevertheless, the photocatalytic degradation efficiency decreases when the catalyst dosage went beyond 1.00 g/L, which can be due to the higher turbidity and the resultant worse transmissivity of the TC solution [63]. Therefore, a modest catalyst dosage is essential to achieve the maximum TC degradation efficiency, and here the photocatalyst dosage located at 0.30 g/L was chosen as the optimal dosage for the following investigations.

3.2.3. Effect of initial TC concentrations

The effect of initial TC concentrations (ranging from 20 to 100 mg/L) on the photodegradation of TC by TCPP$_{0.25}$/rGO/BWO composite is depicted in Fig. 4b. The results clearly show that the higher initial TC concentration leads to a lower TC removal efficiency, where 83.60%, 73.55%, 64.79%, 51.89% and 44.88% of TC were removed at the initial TC concentration of 15, 25, 35, 45 and 55 mg/L, respectively. This phenomenon is mainly attributed to two reasons: (1) the increase of TC concentration reduces the light penetration and prevents the photons from reaching the surface of contaminant molecules [64]; (2) more intermediates are generated and accumulated in the higher TC concentration, which compete with TC molecules for the reactive oxidizing species in the system and inhibit the degradation of TC [65]. Therefore, the appropriate initial concentration is necessary for the photodegradation of TC solution in the practical applications. Herein, 15 mg/L of TC was chosen as the optimal initial concentration throughout the following investigations.

3.2.4. Effect of inorganic anions

It is well-known that various anions exist in wastewater and may affect the photodegradation performance of catalyst [66,67]. Therefore, the effect of inorganic anions on the TC decomposition over TCPP$_{0.25}$/rGO/BWO photocatalyst was investigated by the addition of three model sodium salts (NaNO$_3$, NaCl and Na$_2$CO$_3$) with a concentration of 0.05 M into the TC solution, mainly due to the fact that the photocatalytic degradation process is slightly influenced by the presence of Na$^+$ [68]. As shown in Fig. 4c, NO$_3^-$ and Cl$^-$ had minor effects on the photodegradation of TC, which is probably due to the competition between the anions and the TC molecule for the active sites of TCPP$_{0.25}$/rGO/BWO during the photocatalytic process [69]. In addition, NO$_3^-$ exhibited a weaker suppression effect than Cl$^-$ because the photolysis of NO$_3^-$ can generate a small quantity of ·OH, which to some extent can facilitate the decomposition of TC [70]. However, the addition of CO$_3^{2-}$ can
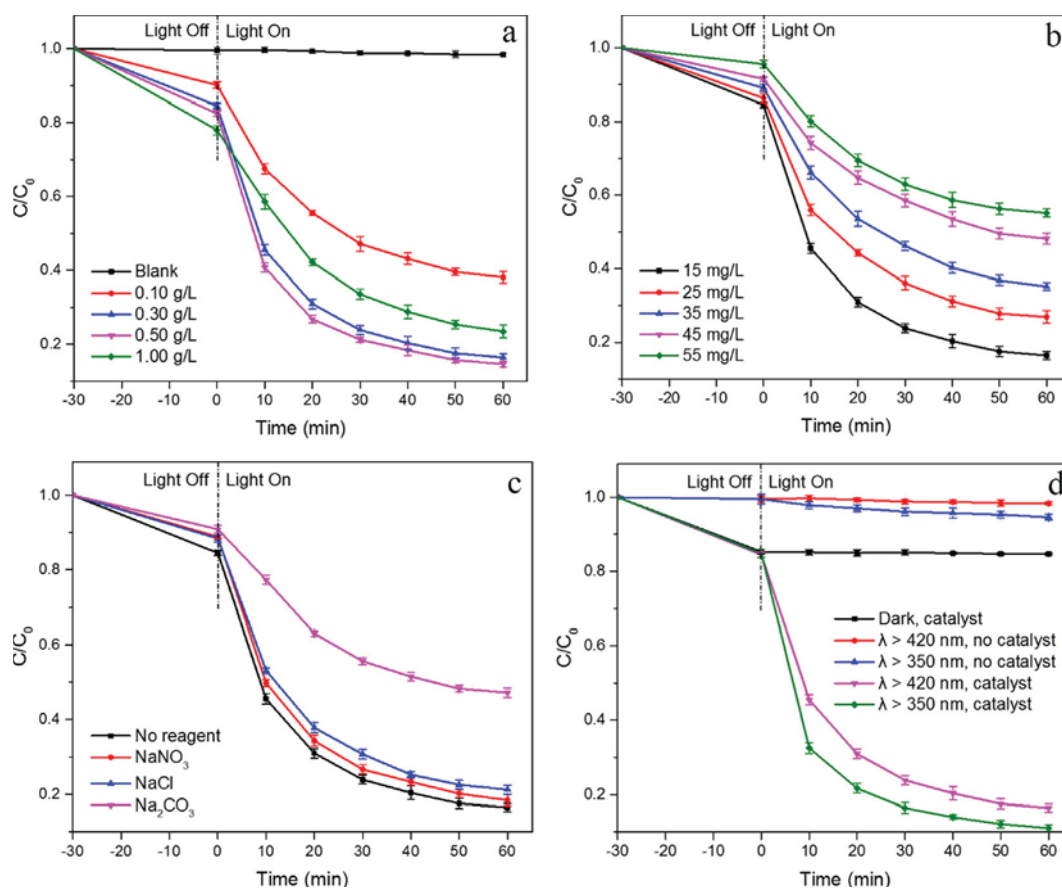
Fig. 4. Effects of (a) photocatalyst dosages, (b) initial TC concentrations, (c) inorganic anions, and (d) light irradiation conditions on the TC photocatalytic performance by TCPP$_{0.25}$/rGO/BWO.

significantly decrease the photodegradation efficiency of TC compared to those of NO_3^- and Cl^- as CO_3^{2-} can act as an effective scavenger of h$^+$, leading to the reduction of photocatalytic performance towards TC degradation [71].

3.2.5. Effect of light irradiation conditions

The energy of photocatalytic reaction comes from the conversion of light energy, so the light irradiation conditions have a significant influence on the photocatalytic performance [72]. Fig. 4d shows the decomposition efficiency of TC over TCPP$_{0.25}$/rGO/BWO photocatalyst within different irradiation conditions by using a 300 W xenon lamp equipped with or without the optical filter. In the dark condition, no obvious decrease of TC concentration was observed after the system reached the adsorption equilibrium within 30 min. More efficient photodegradation reaction of TC (88.97%) was achieved in full spectrum light irradiation without the filter ($\lambda > 350$ nm) as opposed to the degradation process (83.60%) with the filter ($\lambda > 420$ nm). Enhanced TC degradation resulted from the full spectrum light irradiation was also observed without the catalyst. This phenomenon can be attributed to the greater photon energy provided by the light of shorter wavelength. Thus, the experimental data show that TCPP$_{0.25}$/rGO/BWO with excellent absorbency in the entire visible-spectrum exhibits a promising application potential in the disposal of actual water bodies.

3.2.6. The stability of catalyst

Another major concern of the photocatalytic system is the stability and recyclability of the catalyst [73–75]. To investigate the reusability of the TCPP$_{0.25}$/rGO/BWO photocatalyst, recycling experiments were conducted by the photodegradation of TC. As displayed in Fig. 5a, the TC removal efficiency of TCPP$_{0.25}$/rGO/BWO remained 79.27% with only 4.33% decrease after five times of repeated treatment. Moreover, the XRD patterns (Fig. 5b) of TCPP$_{0.25}$/rGO/BWO photocatalyst before and after five cycles of TC photodegradation were characterized, and no obvious changes of the diffraction peaks could be observed, indicating the steady crystal structure. As shown in the SEM image of the post-test sample (Fig. S10), TCPP$_{0.25}$/rGO/BWO still maintained a spherical morphology and a flower-like nanostructure and essentially no obvious changes were observed. In this case, TCPP$_{0.25}$/rGO/BWO exhibits a strong stability in the photocatalytic process and shows a great potential in the real wastewater application.

3.3. Photo-electrochemical properties

Devising photocatalysts with higher separation efficiency of photogenerated charge carriers has always been an important direction in the field of photocatalysis research, because the charge separation efficiency plays a key role in determining the photocatalytic property of the catalyst. The photocurrent response is often used to evaluate the photocatalyst's capability of generating and separating the photoinduced charge carriers. Herein, the photocurrent responses of pristine BWO, rGO/BWO, TCPP/BWO and TCPP$_{0.25}$/rGO/BWO composites are displayed in Fig. S11a. All the BWO composites exhibited higher photocurrent intensity compared with the pristine BWO. Specifically, the TCPP$_{0.25}$/rGO/BWO composites possessed the highest photocurrent density (0.65 μA/cm^2), which is 3.6 times higher than that of pure BWO (0.18 μA/cm^2), 1.9 times of rGO/BWO (0.35 μA/cm^2) and 1.5 times
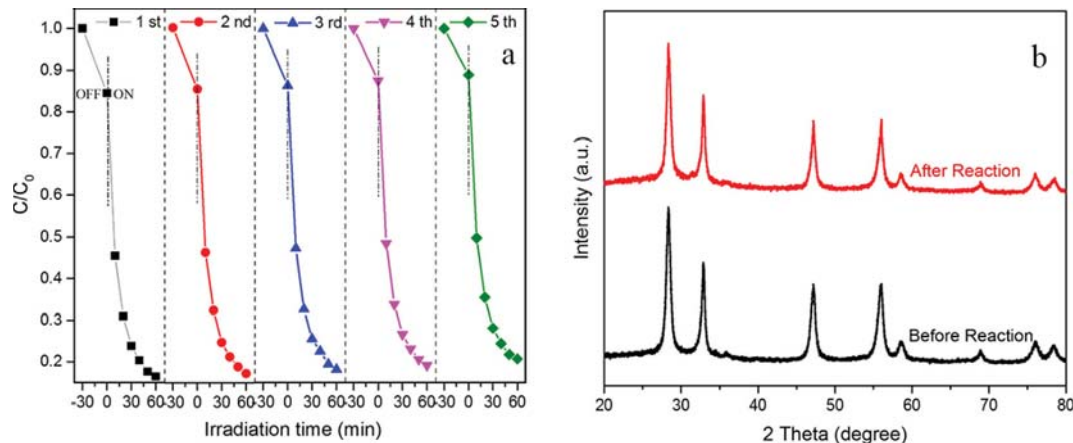
Fig. 5. (a) Recycling experiments for photocatalytic degradation of TC by TCPP$_{0.25}$/rGO/BWO; (b) XRD patterns of the TCPP$_{0.25}$/rGO/BWO before and after the photodegradation reation.

of TCPP/BWO (0.43 µA/cm^2). The result indicates that the incorporation of BWO with rGO and TCPP greatly suppress the recombination of photo-excited charges and highly promote their separation, and the TCPP$_{0.25}$/rGO/BWO heterostructure is successfully constructed by the internal interactions rather than the simple physical mixture of the components.

Electrochemical impedance spectra (EIS) was also carried out to investigate the photo-electrochemical properties of the as-prepared catalysts. Generally, a smaller arc radius represents a higher charge migration and separation rate of sample. As shown in Fig. S11b, the arc radius is in the order of BWO > rGO/BWO > TCPP/BWO > TCPP$_{0.25}$/rGO/BWO, which indicates that the TCPP$_{0.25}$/rGO/BWO has the highest migration and separation efficiency of photoinduced charges. In addition, the EIS result of various photocatalysts has a great consistency with the above photocurrent test and their photocatalytic activity. Therefore, the superior photo-electrochemical properties of TCPP$_{0.25}$/rGO/BWO ternary composite compared to pristine BWO and its binary composites can be categorically proved.

3.4. Mechanisms of enhanced photocatalytic activity

Previous studies show that the h$^+$, ·OH and ·O$_2^-$ radical species are the primary contributors to the photocatalytic decomposition of organic pollutants and play a key role in the process [76,77]. To reveal the photodegradation mechanisms and the predominant

radical species in TCPP$_{0.25}$/rGO/BWO system, the trapping experiments were conducted by using 1.0 mmol of ethylenediaminetetraacetic acid disodium (EDTA-2Na), benzoquinone (BQ) and isopropanol (IPA) as the scavengers of h$^+$, ·O$_2^-$ and ·OH, respectively. As illustrated in Fig. 6, the photocatalytic degradation efficiency of TC did not significantly decrease (from 83.60% to 69.69%) after the addition of IPA, which implies that ·OH is involved but does not play a dominant role in the photodegradation process. However, the presence of EDTA-2Na and BQ greatly suppressed the TC decomposition (from 83.60% to 33.08% and 45.40% for EDTA-2Na and BQ, respectively), suggesting that h$^+$ and ·O$_2^-$ mainly contributed to the TC photodegradation in the TCPP$_{0.25}$/rGO/BWO system.

ESR analysis was carried out to directly prove the generation of ·O$_2^-$ and ·OH in the photocatalytic reaction. As displayed in Fig. S12a, four typical signals of DMPO−·O$_2^-$ for TCPP$_{0.25}$/rGO/BWO are observed when expose to the illumination of visible light, and the signals intensity increases with the prolong of time, while no signals are found in the darkness. Besides, the similar phenomenon is also observed in Fig. S12b, which represents the ESR signals of DMPO−·OH. These results demonstrate the presence of ·O$_2^-$ and ·OH in the TCPP$_{0.25}$/rGO/BWO system [12,78,79], which are consistent with the trapping experiments.

The enhanced photocatalytic activity over TCPP$_{0.25}$/rGO/BWO composites is closely related to the interfacial charge transfer between BWO and TCPP. Based on the energy band structures of
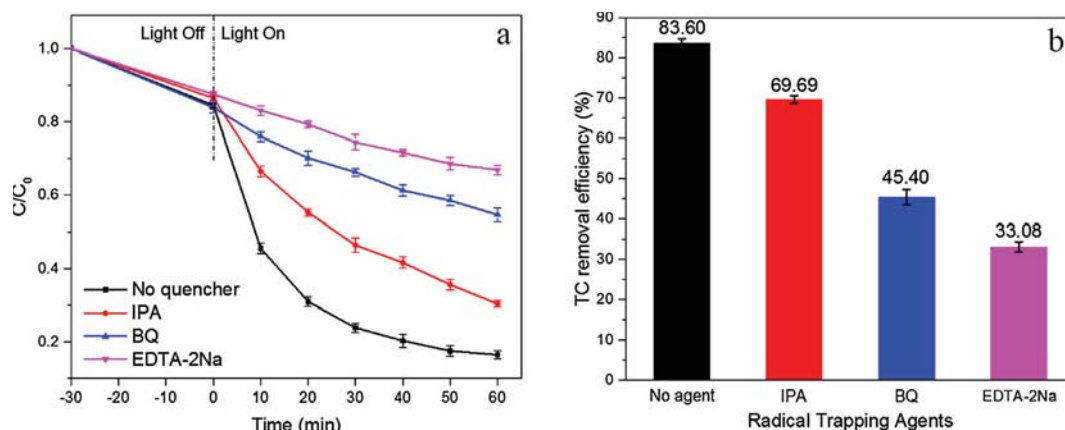

Fig. 6. (a) Trapping experiments of free radicals and (b) comparison results of influences of different tapping agents on TC photodegradation performance by TCPP$_{0.25}$/rGO/BWO.

BWO and TCPP, there are two possible mechanisms to elucidate the charge transfer and TC degradation process in the TCPP$_{0.25}$/rGO/BWO composites. Upon exposing to the visible light, both BWO and TCPP can be excited by the incident photon owing to their narrow band gaps and the electrons on the VB (HOMO) simultaneously jump into the CB (LUMO) and leave the same number of holes in the VB (HOMO), leading to the generation of photoinduced e⁻-h⁺ pairs. In accordance with the common double-transfer mechanism, the photogenerated electrons on the LUMO of TCPP will transfer to the CB of BWO and the resultant photoinduced holes on the VB of BWO will migrate to the HOMO of TCPP. Nevertheless, the CB level of BWO (+0.46 eV) is below the energy level of the O$_2$/·O$_2^-$ redox couple (−0.33 eV), which is thermodynamically unable to reduce O$_2$ to produce ·O$_2^-$ [80]. Similarly, ·OH can't be produced either in the photocatalytic process because the HOMO level of TCPP (+1.10 eV) is beyond the energy level of the OH⁻/·OH redox couple (+2.29 eV) [81]. However, this assumption contradicts with the above-mentioned conclusion that ·O$_2^-$ and ·OH do exist in the TCPP$_{0.25}$/rGO/BWO system, which has been proved by the trapping experiments and ESR analyses. So the common double-transfer mechanism cannot explain the reaction process in the TCPP$_{0.25}$/rGO/BWO system. Herein, we propose another more reasonable Z-scheme mechanism to elucidate the photocatalytic degradation process, and the schematic description is given in Scheme 1. The electrons on the CB of BWO can spontaneously transfer to the HOMO of TCPP because of the formed electric field between them, making BWO and TCPP served as hole-rich and electron-rich reservoir, respectively. For instance, in the previously reported material Bi$_2$Fe$_4$O$_9$/Bi$_2$WO$_6$, electrons in the CB of Bi$_2$WO$_6$ transfer to the VB of Bi$_2$Fe$_4$O$_9$, which has been elucidated by the Z-scheme mechanism in that work [24]. Similar example is also found in Z-scheme BiOI/Ag@AgI heterojunction photocatalysts [82]. In such a way, the photoexcited e⁻-h⁺ pairs can be efficiently separated by the interfacial transfer process between the two components in the Z-scheme TCPP$_{0.25}$/rGO/BWO heterojunction. Besides, the presence of rGO in this Z-scheme system can further promote the separation of charges and suppress their recombination by collecting and shuttling electrons through its unique π-π structure [83]. Thus, the superior photo-electrochemical properties over TCPP$_{0.25}$/rGO/BWO, which has been confirmed by the photocurrent and EIS results, can be rationally explained by the above discussion. The holes accumulated in the VB of BWO then can immediately decompose the TC molecules or oxidize H$_2$O to produce ·OH for TC degradation subsequently because the VB level of BWO (+3.26 eV) is below the energy level of the OH⁻/·OH redox couple (+2.29 eV). At the same time, the electrons accumulated in the LUMO of TCPP can reduce O$_2$ to generate ·O$_2^-$ to degrade TC because the LUMO level of TCPP (−0.60 eV) is higher than the energy level of the O$_2$/·O$_2^-$ redox couple (−0.33 eV). In summary, this photoexcited charge transfer process perfectly match the result of photocurrent, EIS, ESR and trapping experiments, which confirms the successful construction of Z-scheme TCPP$_{0.25}$/rGO/BWO heterojunction.

In addition to the highly efficient charge separation, the considerable improvement of photocatalytic activity over the TCPP$_{0.25}$/rGO/BWO is also the result of the higher photoenergy utilization efficiency and larger surface area. According to the above DRS results, the introduction of rGO and TCPP to BWO greatly broadens the range of light absorption to the entire visible spectrum and increases the absorption intensity, which can further generate more photoinduced e⁻-h⁺ pairs and consequently more free radicals, resulting in the enhanced photocatalytic activity. Moreover, the presence of rGO and TCPP in the TCPP$_{0.25}$/rGO/BWO can highly increase the surface area and pore volume for holding more contaminants and creating bigger reaction interspace, which has been confirmed by the results of BET. Overall, the more efficient charge
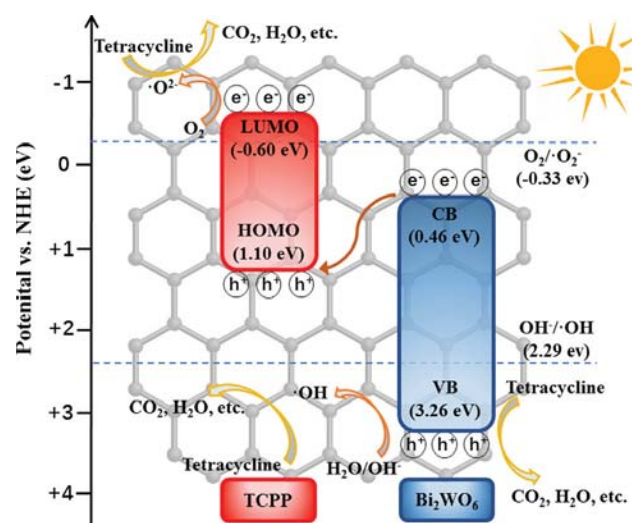
Scheme 1. Schematic diagram of Z-scheme mechanism toward charge transfer and photocatalytic reaction of TCPP$_{0.25}$/rGO/BWO heterojunction photocatalyst.

separation, the better light absorption, and the larger surface area all in together contribute to the remarkably enhanced photocatalytic activity of Z-scheme TCPP$_{0.25}$/rGO/BWO heterojunction towards the degradation of TC.

4. Conclusions

In conclusion, TCPP/rGO/BWO was designed and successfully fabricated as a novel Z-scheme heterojunction photocatalyst for TC removal. The resulting TCPP$_{0.25}$/rGO/BWO photocatalyst has the best photocatalytic performance (removal of 83.60% TC) compared with BWO, rGO/BWO, TCPP/BWO and other TCPP/rGO/BWO composites with different TCPP contents. The hole (h⁺) and superoxide radical (·O$_2^-$) are the major contributors for the TC decomposition in the TCPP$_{0.25}$/rGO/BWO system according to the results of trapping experiments and ESR analysis. Additionally, the TCPP$_{0.25}$/rGO/BWO photocatalyst has a great recyclability and stability, as it still had high removal efficiency for TC (79.27%) even after being used for five times. A Z-scheme mechanism is proposed to elucidate the charge transfer process in the TCPP$_{0.25}$/rGO/BWO ternary composite, in which BWO and TCPP serve as the hole-rich and electron-rich reservoir respectively and hence the photoexcited e⁻-h⁺ pairs can be efficiently separated. The key improvements of this work are: (1) a facile method combining hydrothermal approach with liquid ultrasonic route was developed to synthesize ternary TCPP/rGO/BWO composites; (2) compared to the widely studied graphene/BWO composites, the ternary Z-scheme TCPP/rGO/BWO composites with low TCPP content can significantly enhance the photocatalytic activity of the material (from 66.93% to 83.60% for TC removal efficiency); (3) while the previous works mainly focused on the investigation of photocatalytic degradation of organic dyes (e.g., RhB) by using graphene/BWO-based composites, a more recalcitrant antibiotic (e.g., TC) was degraded by a novel TCPP/rGO/BWO material; and (4) the enhanced photocatalytic performance of TCPP$_{0.25}$/rGO/BWO is systematically elaborated from three aspects (i.e. more efficient charge separation, better light absorption, and larger surface area), which are confirmed by characterizations such as photocurrent, EIS, DRS and BET. This work provides a new insight for novel photocatalysts preparation by combining porphyrin and semiconductor that have matching energy band structure and promote their application in antibiotic wastewater treatment.

Acknowledgements

Appendix A. Supplementary material

Supplementary data to this article can be found online at https://doi.org/10.1016/j.jcis.2019.01.013.

References

[1] G. Zeng, M. Chen, Z. Zeng, Shale gas: surface water also at risk, Nature 499 (2013) 154.

[2] S. Ye, G. Zeng, H. Wu, C. Zhang, J. Liang, J. Dai, Z. Liu, W. Xiong, J. Wan, P. Xu, Co-occurrence and interactions of pollutants, and their impacts on soil remediation—a review, Crit. Rev. Env. Sci. Tec. 47 (2017) 1528–1553.

[3] Y. Wang, Y. Zhu, Y. Hu, G. Zeng, Y. Zhang, C. Zhang, C. Feng, How to construct DNA hydrogels for environmental applications: advanced water treatment and environmental analysis, Small 1703305 (2018).

[4] X. Ren, G. Zeng, L. Tang, J. Wang, J. Wan, Y. Liu, J. Yu, H. Yi, S. Ye, R. Deng, Sorption, transport and biodegradation - an insight into bioavailability of persistent organic pollutants in soil, Sci. Total Environ. 610–611 (2018) 1154–1163.

[5] X. Ren, G. Zeng, L. Tang, J. Wang, J. Wan, H. Feng, B. Song, C. Huang, X. Tang, Effect of exogenous carbonaceous materials on the bioavailability of organic pollutants and their ecological risks, Soil Biol. Biochem. 116 (2018) 70–81.

[6] Y. Ye, Z. Zang, T. Zhou, F. Dong, S. Lu, X. Tang, W. Wei, Y. Zhang, Theoretical and experimental investigation of highly photocatalytic performance of CuInZnS nanoporous structure for removing the NO gas, J. Catal. 357 (2018) 100–107.

[7] C.-C. Wang, J.-R. Li, X.-L. Lv, Y.-Q. Zhang, G. Guo, Photocatalytic organic pollutants degradation in metal–organic frameworks, Energ. Environ. Sci. 7 (2014) 2831–2867.

[8] S. Chuangchote, J. Jitputti, T. Sagawa, S. Yoshikawa, Photocatalytic activity for hydrogen evolution of electrospun TiO2 nanofibers, ACS Appl. Mater. Inter. 1 (2009) 1140.

[9] A. Fujishima, K. Honda, Electrochemical photolysis of water at a semiconductor electrode, Nature 238 (1972) 37–38.

[10] C. Sun, Y. Wu, W. Zhang, N. Jiang, T. Jiu, J. Fang, Improving efficiency by hybrid TiO2 nanorods with 1,10-phenanthroline as a cathode buffer layer for inverted organic solar cells, ACS Appl. Mater. Inter. 6 (2014) 739–744.

[11] H. Dong, G. Zeng, L. Tang, C. Fan, C. Zhang, X. He, Y. He, An overview on limitations of TiO2-based particles for photocatalytic degradation of organic pollutants and the corresponding countermeasures, Water Res. 79 (2015) 128–146.

[12] S. Li, X. Shen, J. Liu, L. Zhang, Synthesis of Ta3N5/Bi2MoO6 core–shell fiber-shaped heterojunctions as efficient and easily recyclable photocatalysts, Environ. Sci. Nano 4 (2017) 1155–1167.

[13] S. Li, S. Hu, W. Jiang, Y. Liu, J. Liu, Z. Wang, Facile synthesis of flower-like Ag3VO4/Bi2WO6 heterojunction with enhanced visible-light photocatalytic activity, J. Colloid Interf. Sci. 501 (2017) 156–163.

[14] S. Li, S. Hu, W. Jiang, Y. Liu, Y. Zhou, J. Liu, Z. Wang, Facile synthesis of cerium oxide nanoparticles decorated flower-like bismuth molybdate for enhanced photocatalytic activity toward organic pollutant degradation, J. Colloid Interf. Sci. 530 (2018) 171–178.

[15] S. Li, S. Hu, K. Xu, W. Jiang, J. Liu, Z. Wang, A novel heterostructure of BiOI nanosheets anchored onto MWCNTs with excellent visible-light photocatalytic activity, Nanomaterials 7 (2017) 22.

[16] D. Ma, J. Wu, M. Gao, Y. Xin, T. Ma, Y. Sun, Fabrication of Z-scheme g-C3N4/RGO/Bi2WO6 photocatalyst with enhanced visible-light photocatalytic activity, Chem. Eng. J. 290 (2016) 136–146.

[17] M. Li, L. Zhang, X. Fan, Y. Zhou, M. Wu, J. Shi, Highly selective CO2 photoreduction to CO over g-C3N4/Bi2WO6 composites under visible light, J. Mater. Chem. A 3 (2015) 5189–5196.

[18] J.J. Wang, L. Tang, G. Zeng, Y. Liu, Y. Zhou, Y. Deng, J. Wang, B. Peng, Plasmonic Bi metal deposition and g-C3N4 coating on Bi2WO6 microspheres for efficient visible light photocatalysis, ACS Sustain. Chem. Eng. 5 (2017) 1062–1072.

[19] Z. Zhang, W. Wang, L. Wang, S. Sun, Enhancement of visible-light photocatalysis by coupling with narrow-band-gap semiconductor: a case study on Bi2S3/Bi2WO6, ACS Appl. Mater. Inter. 4 (2012) 593.

[20] D. He, L. Wang, D. Xu, J. Zhai, D. Wang, T. Xie, Investigation of photocatalytic activities over Bi2WO6/ZnWO4 composite under UV light and its photoinduced charge transfer properties, ACS Appl. Mater. Inter. 3 (2011) 3167–3171.

[21] F. Ma, Q. Yang, Z. Wang, Y. Liu, J. Xin, J. Zhang, Y. Hao, L. Li, Enhanced visible-light photocatalytic activity and photostability of Ag3PO4/Bi2WO6

[22] C. Zhou, C. Lai, C. Zhang, G. Zeng, D. Huang, M. Cheng, L. Hu, W. Xiong, M. Chen, J. Wang, Y. Yang, L. Jiang, Semiconductor/boron nitride composites: synthesis, properties, and photocatalysis applications, Appl. Catal. B: Environ. 238 (2018) 6–18.

[23] W. Xiong, Z. Zeng, X. Li, G. Zeng, R. Xiao, Z. Yang, Y. Zhou, C. Zhang, M. Cheng, L. Hu, C. Zhou, L. Qin, R. Xu, Y. Zhang, Multi-walled carbon nanotube/amino-functionalized MIL-53(Fe) composites: remarkable adsorptive removal of antibiotics from aqueous solutions, Chemosphere 210 (2018) 1061–1069.

[24] B. Li, C. Lai, G. Zeng, L. Qin, H. Yi, D. Huang, C. Zhou, X. Liu, M. Cheng, P. Xu, C. Zhang, F. Huang, S. Liu, Facile hydrothermal synthesis of Z-scheme Bi2Fe4O9/Bi2WO6 heterojunction photocatalyst with enhanced visible light photocatalytic activity, ACS Appl. Mater. Inter. 10 (2018) 18824–18836.

[25] M.M. Maitani, C. Zhan, M. Dai, E. Suzuki, Y. Wada, Influence of co-existing alcohol on charge transfer of H2 evolution under visible light with dye-sensitized nanocrystalline TiO2, Appl. Catal. B: Environ. 140–141 (2013) 406–411.

[26] J. Wan, M. Wei, Z. Hu, Z. Peng, B. Wang, D. Feng, Y. Shen, Ternary composites of TiO2 nanotubes with reduced graphene oxide (rGO) and meso-tetra (4-carboxyphenyl) porphyrin for enhanced visible light photocatalysis, Int. J. Hydrogen Energy 41 (2016) 14692–14703.

[27] Y.J. Yuan, J.R. Tu, Z.J. Ye, H.W. Lu, Z.G. Ji, B. Hu, Y.H. Li, D.P. Cao, Z.T. Yu, Z.G. Zou, Visible-light-driven hydrogen production from water in a noble-metal-free system catalyzed by zinc porphyrin sensitized MoS2/ZnO, Dyes Pigments 123 (2015) 285–292.

[28] H. Yi, M. Jiang, D. Huang, G. Zeng, C. Lai, L. Qin, C. Zhou, B. Li, X. Liu, M. Cheng, Advanced photocatalytic Fenton-like process over biomimetic hemin-Bi2WO6 with enhanced pH, J. Taiwan. Inst. of Chem. E. 93 (2018) 184–192.

[29] B. Zhuang, L. Xiangqing, R. Ge, S. Kang, L. Qin, G. Li, Assembly and electron transfer mechanisms on visible light responsive 5,10,15,20-meso-tetra(4-carboxyphenyl)porphyrin/cuprous oxide composite for photocatalytic hydrogen production, Appl. Catal. A: Gen. 533 (2017) 81–89.

[30] Y. Wang, J. Yu, W. Xiao, Q. Li, Microwave-assisted hydrothermal synthesis of graphene based Au–TiO2 photocatalysts for efficient visible-light hydrogen production, J. Mate. Chem. A 2 (2014) 3847–3855.

[31] K. He, G. Chen, G. Zeng, A. Chen, Z. Huang, J. Shi, T. Huang, M. Peng, L. Hu, Three-dimensional graphene supported catalysts for organic dyes degradation, Appl. Catal. B: Environ. 228 (2018) 19–28.

[32] K. He, Z. Zeng, A. Chen, G. Zeng, R. Xiao, P. Xu, Z. Huang, J. Shi, L. Hu, G. Chen, Advancement of Ag-graphene based nanocomposites: an overview of synthesis and its applications, Small 1800871 (2018).

[33] H. Yi, D. Huang, L. Qin, G. Zeng, C. Lai, M. Cheng, S. Ye, B. Song, X. Ren, X. Guo, Selective prepared carbon nanomaterials for advanced photocatalytic application in environmental pollutant treatment and hydrogen production, Appl. Catal. B: Environ. 239 (2018) 408–424.

[34] A. Reheman, K. Kadeer, K. Okitsu, M. Halidan, Y. Tursun, T. Dilinuer, A. Abulikemu, Facile photo-ultrasonic assisted reduction for preparation of rGO/Ag2CO3 nanocomposites with enhanced photocatalytic oxidation activity for tetracycline, Ultrason. Sonochem. 51 (2018) 166–177.

[35] W. Wang, H. Wang, W. Zhang, H. Liang, D. Gao, Occurrence, distribution, and risk assessment of antibiotics in the Songhua River in China, Environ. Sci. Pollut. R. 24 (2017) 19282–19292.

[36] S. Dong, X. Ding, T. Guo, X. Yue, X. Han, J. Sun, Self-assembled hollow sphere shaped Bi2WO6/RGO composites for efficient sunlight-driven photocatalytic degradation of organic pollutants, Chem. Eng. J. 316 (2017) 778–789.

[37] E. Gao, W. Wang, M. Shang, J. Xu, Synthesis and enhanced photocatalytic performance of graphene-Bi2WO6 composite, Phys. Chem. Chem. Phys. 13 (2011) 2887–2893.

[38] J. Zhai, H. Yu, H. Li, L. Sun, K. Zhang, H. Yang, Visible-light photocatalytic activity of graphene oxide-wrapped Bi2WO6 hierarchical microspheres, Appl. Surf. Sci. 344 (2015) 101–106.

[39] C. Chen, S. Cao, W. Yu, X. Xie, Q. Liu, Y. Tsang, Y. Xiao, Adsorption, photocatalytic and sunlight-driven antibacterial activity of Bi2WO6/graphene oxide nanoflakes, Vacuum 116 (2015) 48–53.

[40] X. Xu, F. Ming, J. Hong, Y. Xie, Z. Wang, Three-dimensional porous aerogel constructed by Bi2WO6 nanosheets and graphene with excellent visible-light photocatalytic performance, Mater. Lett. 179 (2016) 52–56.

[41] H. Lv, Y. Liu, J. Hu, Z. Li, Y. Lu, Ionic liquid-assisted hydrothermal synthesis of Bi2WO6–reduced graphene oxide composites with enhanced photocatalytic activity, RSC Adv. 4 (2014) 63238–63245.

[42] M. Liu, X. Xue, S. Yu, X. Wang, X. Hu, H. Tian, H. Chen, W. Zheng, Improving photocatalytic performance from Bi2WO6@MoS2/graphene hybrids via gradual charge transferred pathway, Sci. Rep. 7 (2017) 3637.

[43] D.C.T. Nguyen, K.Y. Cho, W.-C. Oh, New synthesis of the ternary type Bi2WO6-GO-TiO2 nanocomposites by the hydrothermal method for the improvement of the photo-catalytic effect, Appl. Chem. Eng. 28 (2017) 705–713.

[44] J. Low, J. Yu, Q. Li, B. Cheng, Enhanced visible-light photocatalytic activity of plasmonic Ag and graphene co-modified Bi2WO6 nanosheets, Phys. Chem. Chem. Phys. 16 (2014) 1111–1120.

[45] J. Yang, X. Wang, X. Zhao, J. Dai, S. Mo, Synthesis of uniform Bi2WO6-reduced graphene oxide nanocomposites with significantly enhanced photocatalytic reduction activity, J. Phys. Chem. C 119 (2015) 3068–3078.

[46] T. Wang, C. Li, J. Ji, Y. Wei, P. Zhang, S. Wang, X. Fan, J. Gong, Reduced graphene oxide (rGO)/BiVO$_4$ composites with maximized interfacial coupling for visible light photocatalysis, ACS Sustain. Chem. Eng. 2 (2014) 2253–2258.

[47] L. Zhang, W. Wang, Z. Chen, L. Zhou, H. Xu, W. Zhu, Fabrication of flower-like Bi$_2$WO$_6$ superstructures as high performance visible-light driven photocatalysts, J. Mate. Chem. 17 (2007) 2526–2532.

[48] H. Ji, F. Chang, X. Hu, Q. Wei, J. Shen, Photocatalytic degradation of 2,4,6-trichlorophenol over g-C$_3$N$_4$ under visible light irradiation, Chem. Eng. J. 218 (2013) 183–190.

[49] P. Tang, H. Chen, F. Cao, One-step preparation of bismuth tungstate nanodisks with visible-light photocatalytic activity, Mater. Lett. 68 (2012) 171–173.

[50] Y. Yuan, H. Lu, Z. Ji, J. Zhong, M. Ding, D. Chen, Y. Li, W. Tu, D. Cao, Z. Yu, Enhanced visible-light-induced hydrogen evolution from water in a noble-metal-free system catalyzed by ZnTCPP-MoS2/TiO$_2$ assembly, Chem. Eng. J. 275 (2015) 8–16.

[51] G. Huang, W.L. Wang, X.X. Ning, Y. Liu, S.K. Zhao, Y.A. Guo, S.J. Wei, H. Zhou, Interesting green catalysis of cyclohexane oxidation over metal tetrakis(4-carboxyphenyl)porphyrins promoted by zinc sulfide, Ind. Eng. Chem. Res. 55 (2016) 2959–2969.

[52] X. Qian, D. Yue, Z. Tian, R. Meng, Y. Zhu, M. Kan, T. Zhang, Y. Zhao, Carbon quantum dots decorated Bi$_2$WO$_6$ nanocomposite with enhanced photocatalytic oxidation activity for VOCs, Appl. Catal. B: Environ. 193 (2016) 16–21.

[53] Y. Guo, L. Chen, X. Yang, F. Ma, S. Zhang, Y. Yang, Y. Guo, X. Yuan, Visible light-driven degradation of tetrabromobisphenol A over heterostructured Ag/Bi$_5$Nb$_3$O$_{15}$ materials, RSC Adv. 2 (2012) 4656–4663.

[54] X. Miao, X. Yue, X.P. Shen, Z.Y. Ji, H. Zhou, G. Zhu, J. Wang, L. Kong, M. Liu, C. Song, Nitrogen-doped carbon dots modified Ag$_3$PO$_4$/GO photocatalyst with excellent visible-light-driven photocatalytic performance and mechanism insight, Catal. Sci. Technol. 8 (2018) 632–641.

[55] Y. Wang, J. Wang, H. Shen, P. Huo, C. Li, Y. Yan, W. Shi, Synthesis of Ag$_3$PO$_4$/RGO/Bi$_2$WO$_6$ composites with highly efficient photocatalytic activity: efficient visible-light driven all-solid-state Z-scheme photocatalyst, Nano 12 (2017) 1750149.

[56] K.S. Sing, Reporting physisorption data for gas/solid systems with special reference to the determination of surface area and porosity (Recommendations 1984), Pure. Appl. Chem. 57 (1985) 603–619.

[57] Z. Sun, J. Guo, S. Zhu, J. Ma, Y. Liao, D. Zhang, High photocatalytic performance by engineering Bi$_2$WO$_6$ nanoneedles onto graphene sheets, RSC Adv. 4 (2014) 27963–27970.

[58] X. Xin, J. Lang, T. Wang, Y. Su, Y. Zhao, X. Wang, Construction of novel ternary component photocatalyst Sr0. 25H1. 5Ta2O6·H2O coupled with g-C$_3$N$_4$ and Ag toward efficient visible light photocatalytic activity for environmental remediation, Appl. Catal. B: Environ. 181 (2016) 197–209.

[59] H. Che, C. Liu, W. Hu, H. Hu, J. Li, J. Dou, W. Shi, C. Li, H. Dong, NGQD active sites as effective collectors of charge carriers for improving the photocatalytic performance of Z-scheme g-C$_3$N$_4$/Bi$_2$WO$_6$ heterojunctions, Catal. Sci. Technol. 8 (2018) 622–631.

[60] W.-K. Jo, J.Y. Lee, T.S. Natarajan, Fabrication of hierarchically structured novel redox-mediator-free ZnIn$_2$S$_4$ marigold flower/Bi$_2$WO$_6$ flower-like direct Z-scheme nanocomposite photocatalysts with superior visible light photocatalytic efficiency, Phys. Chem. Chem. Phys. 18 (2016) 1000–1016.

[61] F. Chen, Q. Yang, J. Sun, F. Yao, S. Wang, Y. Wang, X. Wang, X. Li, C. Niu, D. Wang, Enhanced photocatalytic degradation of tetracycline by AgI/BiVO$_4$ heterojunction under visible-light irradiation: mineralization efficiency and mechanism, ACS Appl. Mater. Inter. 8 (2016) 32887–32900.

[62] Y. Guo, G. Zhang, J. Liu, Y. Zhang, Hierarchically structured α-Fe$_2$O$_3$/Bi$_2$WO$_6$ composite for photocatalytic degradation of organic contaminants under visible light irradiation, RSC Adv. 3 (2013) 2963–2970.

[63] F. Chen, Q. Yang, C. Niu, X. Li, C. Zhang, J. Zhao, Q. Xu, Y. Zhong, Y. Deng, G. Zeng, Enhanced visible light photocatalytic activity and mechanism of ZnSn(OH)$_6$ nanocubes modified with AgI nanoparticles, Catal. Commun. 73 (2016) 1–6.

[64] H. Wang, X. Yuan, Y. Wu, G. Zeng, X. Chen, L. Leng, Z. Wu, L. Jiang, H. Li, Facile synthesis of amino-functionalized titanium metal-organic frameworks and their superior visible-light photocatalytic activity for Cr(VI) reduction, J. Hazard. Mater. 286 (2015) 187–194.

[65] B. Zhou, X. Zhao, H. Liu, J. Qu, C.P. Huang, Visible-light sensitive cobalt-doped BiVO4 (Co-BiVO4) photocatalytic composites for the degradation of methylene blue dye in dilute aqueous solutions, Appl. Catal. B: Environ. 99 (2010) 214–221.

[66] J.L. Gong, B. Wang, G.M. Zeng, C.P. Yang, C.G. Niu, Q.Y. Niu, W.J. Zhou, Y. Liang, Removal of cationic dyes from aqueous solution using magnetic multi-wall carbon nanotube nanocomposite as adsorbent, J. Hazard. Mater. 164 (2009) 1517–1522.

[67] L. Zhang, J. Zhang, G. Zeng, H. Dong, Y. Chen, H. Chao, Z. Yuan, X. Rui, Y. Cheng, K. Hou, Multivariate relationships between microbial communities and environmental variables during co-composting of sewage sludge and agricultural waste in the presence of PVP-AgNPs, Bioresource Technol. 261 (2018) 10.

[68] X.J. Wen, C.G. Niu, L. Zhang, G. Zeng, Fabrication of SnO$_2$ nanopaticles/BiOI n–p heterostructure for wider spectrum visible-light photocatalytic degradation of antibiotic oxytetracycline hydrochloride, ACS Sustain. Chem. Eng. 5 (2017).

[69] F. Chen, Q. Yang, Y. Wang, J. Zhao, D. Wang, X. Li, Z. Guo, H. Wang, Y. Deng, C. Niu, Novel ternary heterojunction photcocatalyst of Ag nanoparticles and g-C$_3$N$_4$ nanosheets co-modified BiVO$_4$ for wider spectrum visible-light photocatalytic degradation of refractory pollutant, Appl. Catal. B: Environ. 205 (2017) 133–147.

[70] H. Fu, C. Pan, A. Wenqing Yao, Y. Zhu, Visible-light-induced degradation of rhodamine B by nanosized Bi2WO6, J. Phys. Chem. C 109 (2005) 22432.

[71] H. Xiao, R. Liu, X. Zhao, J. Qu, Enhanced degradation of 2,4-dinitrotoluene by ozonation in the presence of manganese(II) and oxalic acid, J. Mol. Catal. A: Chem. 286 (2008) 149–155.

[72] Y. Yang, C. Zhang, C. Lai, G. Zeng, D. Huang, M. Cheng, J. Wang, F. Chen, C. Zhou, W. Xiong, BiOX (X = Cl, Br, I) photocatalytic nanomaterials: applications for fuels and environmental management, Adv. Colloid Interface 254 (2018) 76–93.

[73] P. Xu, G.M. Zeng, D.L. Huang, C.L. Feng, S. Hu, M.H. Zhao, C. Lai, Z. Wei, C. Huang, G.X. Xie, Use of iron oxide nanomaterials in wastewater treatment: a review, Sci. Total Environ. 424 (2012) 1–10.

[74] Z. Huang, K. He, Z. Song, G. Zeng, A. Chen, L. Yuan, H. Li, L. Hu, Z. Guo, G. Chen, Antioxidative response of Phanerochaete chrysosporium against silver nanoparticle-induced toxicity and its potential mechanism, Chemosphere 211 (2018) 573–583.

[75] L. Qin, G. Zeng, C. Lai, D. Huang, P. Xu, C. Zhang, M. Cheng, X. Liu, S. Liu, B. Li, Gold rush" in modern science: fabrication strategies and typical advanced applications of gold nanoparticles in sensing, Coordin. Chem. Rev. 359 (2018) 1–31.

[76] L. Tang, J. Wang, G. Zeng, Y. Liu, Y. Deng, Y. Zhou, J. Tang, J. Wang, Z. Guo, Enhanced photocatalytic degradation of norfloxacin in aqueous Bi$_2$WO$_6$ dispersions containing nonionic surfactant under visible light irradiation, J. Hazard. Mater. 306 (2016) 295–304.

[77] X. Tang, G. Zeng, C. Fan, M. Zhou, L. Tang, J. Zhu, J. Wan, D. Huang, M. Chen, P. Xu, Chromosomal expression of CadR on Pseudomonas aeruginosa for the removal of Cd(II) from aqueous solutions, Sci. Total Environ. 636 (2018) 1355.

[78] F. Chen, Q. Yang, Y. Wang, F. Yao, Y. Ma, X. Huang, X. Li, D. Wang, G. Zeng, H. Yu, Efficient construction of bismuth vanadate-based Z-scheme photocatalyst for simultaneous Cr (VI) reduction and ciprofloxacin oxidation under visible light: kinetics, degradation pathways and mechanism, Chem. Eng. J. 348 (2018) 157–170.

[79] J. Yang, D. Chen, Y. Zhu, Y. Zhang, Y. Zhu, 3D–3D porous Bi$_2$WO$_6$/graphene hydrogel composite with excellent synergistic effect of adsorption-enrichment and photocatalytic degradation, Appl. Catal. B: Environ. 205 (2017) 228–237.

[80] Y. Yang, Z. Zeng, C. Zhang, D. Huang, G. Zeng, R. Xiao, C. Lai, C. Zhou, H. Guo, W. Xue, Construction of iodine vacancy-rich BiOI/Ag@AgI Z-scheme heterojunction photocatalysts for visible-light-driven tetracycline degradation: transformation pathways and mechanism insight, Chem. Eng. J. 349 (2018) 808–821.

[81] W.K. Jo, T.S. Natarajan, Influence of TiO$_2$ morphology on the photocatalytic efficiency of direct Z-scheme g-C$_3$N$_4$/TiO$_2$ photocatalysts for isoniazid degradation, Chem. Eng. J. 281 (2015) 549–565.

[82] Y. Yang, Z. Zeng, C. Zhang, D. Huang, G. Zeng, R. Xiao, C. Lai, C. Zhou, H. Guo, W. Xue, M. Cheng, W. Wang, J. Wang, Construction of iodine vacancy-rich BiOI/Ag@AgI Z-scheme heterojunction photocatalysts for visible-light-driven tetracycline degradation: Transformation pathways and mechanism insight, Chem. Eng. J. 349 (2018) 808–821.

[83] J. Wang, P. Wang, Y. Cao, J. Chen, W. Li, Y. Shao, Y. Zheng, D. Li, A high efficient photocatalyst Ag$_3$VO$_4$/TiO$_2$/graphene nanocomposite with wide spectral response, Appl. Catal. B: Environ. 136 (2013) 94–102.